Supplementary Materials for

Tunable Room-temperature Ferromagnetism in two-dimensional Cr_2Te_3

Yao Wen[†,1], Zhehong Liu[†,2], Yu Zhang[1], Congxin Xia[4], Baoxing Zhai[4], Xinhui Zhang[5], Guihao Zhai[5], Chao Shen[5], Peng He[3], Ruiqing Cheng[3], Lei Yin[3], Yuyu Yao[3], Marshet Getaye Sendeku[3], Zhenxing Wang[3], Xubing Ye[2], Chuansheng Liu,[1] Chao Jiang[3], Chongxin Shan[7], Youwen Long*[,2,6], Jun He*[,1]

[1]School of Physics and Technology, Wuhan University, Wuhan 430072, China

[2]Beijing National Laboratory for Condensed Matter Physics, Institute of Physics, University of Chinese Academy of Sciences, Beijing 100049, China

[3]CAS Center for Excellence in Nanoscience, National Center for Nanoscience and Technology, University of Chinese Academy of Sciences, Beijing 100049, China

[4]Department of Physics, Henan Normal University, Xinxiang 453007, China

[5]State Key Laboratory of Superlattices and Microstructures, Institute of Semiconductors, University of Chinese Academy of Sciences, Beijing, 100049, China

[6]Songshan Lake Materials Laboratory, Dongguan, Guangdong 523808, China

[7]Henan Key Laboratory of Diamond Optoelectronic Materials and Devices, School of Physics and Engineering, Zhengzhou University, Zhengzhou, 450052, China

[†]These authors contribute equally to this work

* Correspondence to: hej@nanoctr.cn; ywlong@iphy.ac.cn

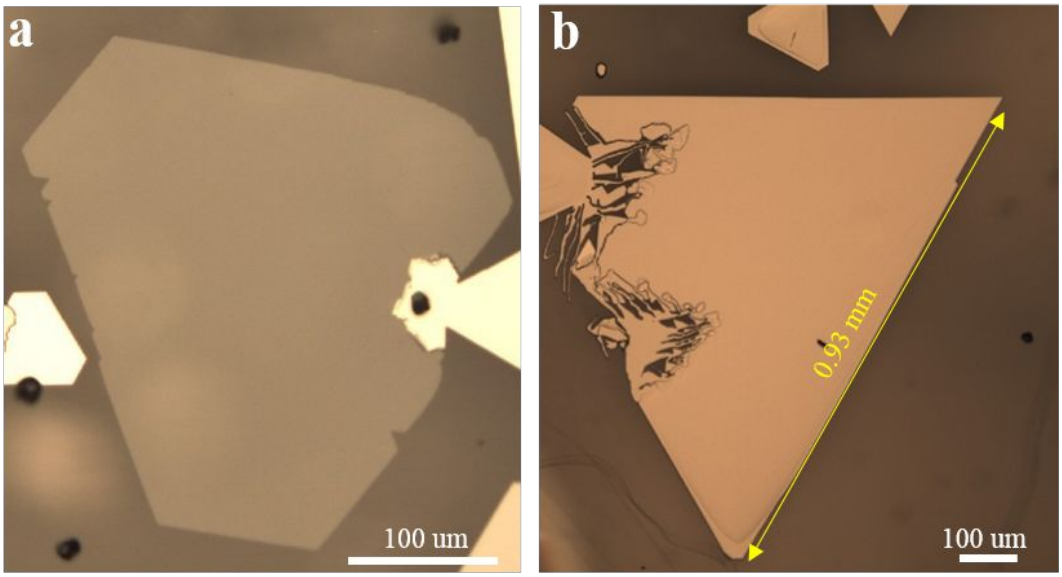

Figure S1. (a,b) Optical micrographs of CVD grown Cr_2Te_3 exhibit large size. Millimeter-scale (over 0.93 mm) Cr_2Te_3 has been achieved.

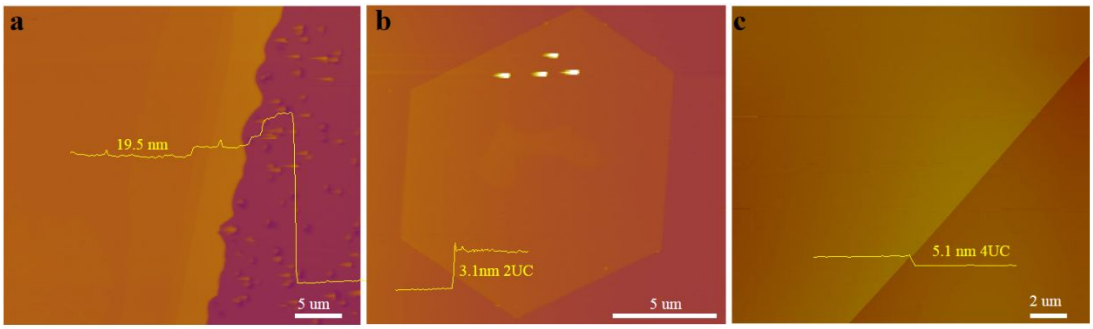

Figure S2. (a,b,c) AFM images and height profile of CVD grown Cr_2Te_3.

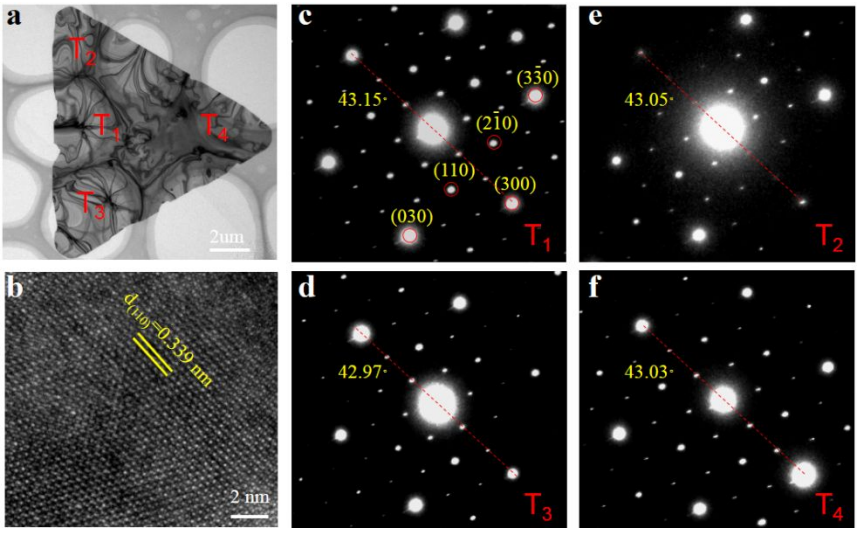

Figure S3. (a) TEM image of a representative Cr_2Te_3 domain on TEM grid. (b)

HRTEM image indicates the lattice constant (110) with 0.339 nm. (c-f) SAED patterns acquired from the labelled areas of the same triangular Cr_2Te_3 in (a).

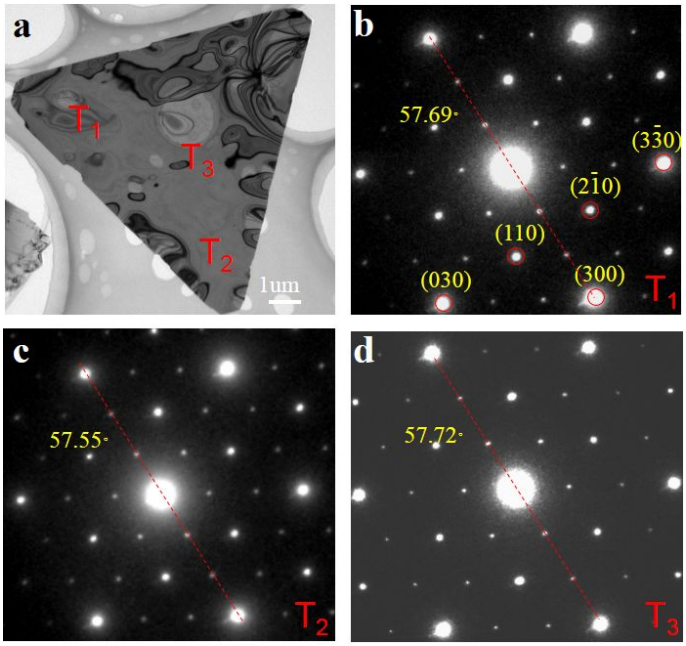

Figure S4. (a) TEM image of a representative Cr_2Te_3 domain on TEM grid. (b-d) SAED patterns acquired from the labelled areas of the same triangular Cr_2Te_3 in (a).

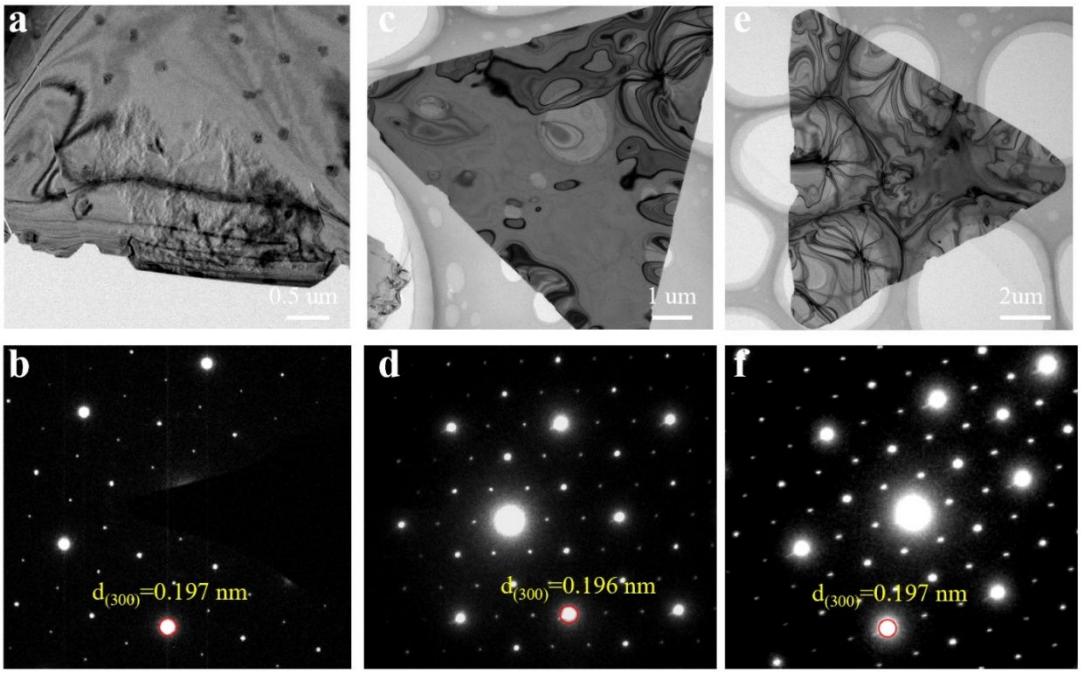

Figure S5. (a, c, e) TEM image of a representative Cr_2Te_3 domain on TEM grid. (b, d, f) SAED patterns of the triangular Cr_2Te_3.

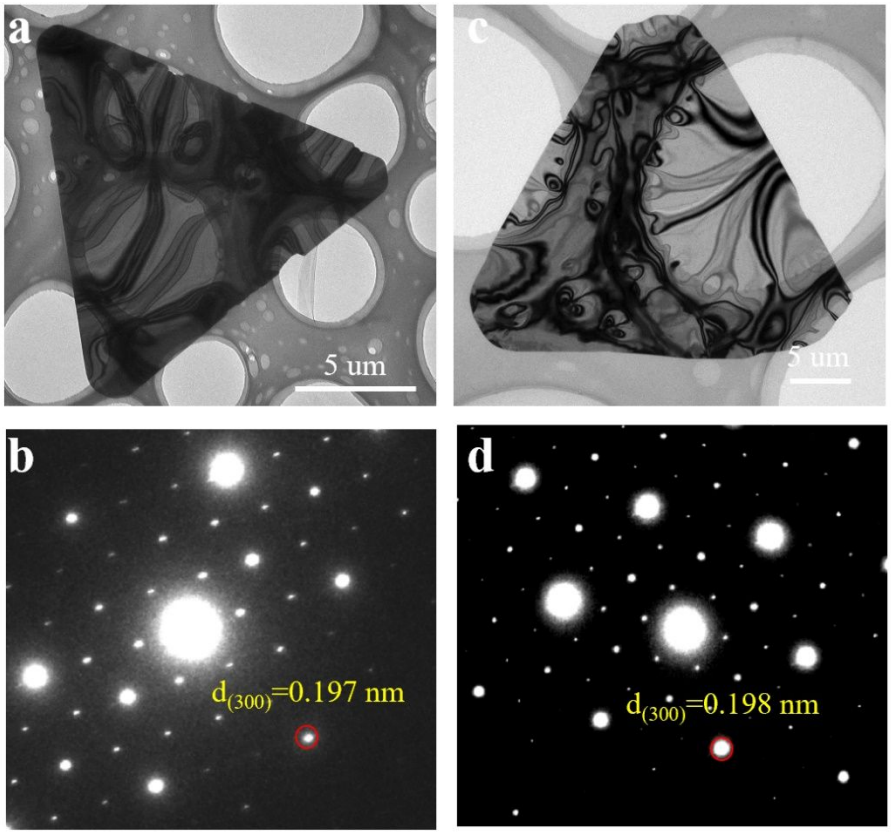

Figure S6. (a, c) TEM image of a representative Cr_2Te_3 domain on TEM grid. (b, d) SAED patterns of the triangular Cr_2Te_3.

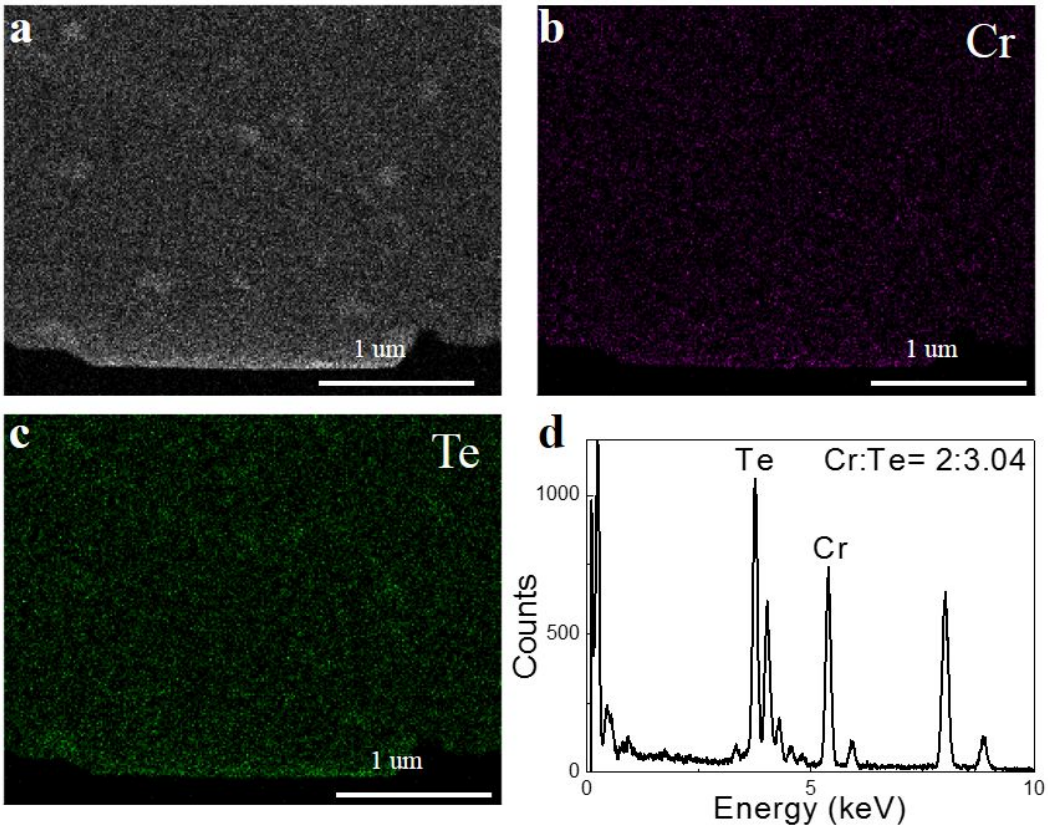

Figure S7. (a) TEM image of Cr_2Te_3 domain on TEM grid. (b, c) The distribution of Cr and Te elements via TEM-EDX mapping. There is no indication that the Cr or Te element is concentrated at the surface. (d) The chemical composition analysis of TEM-EDX.

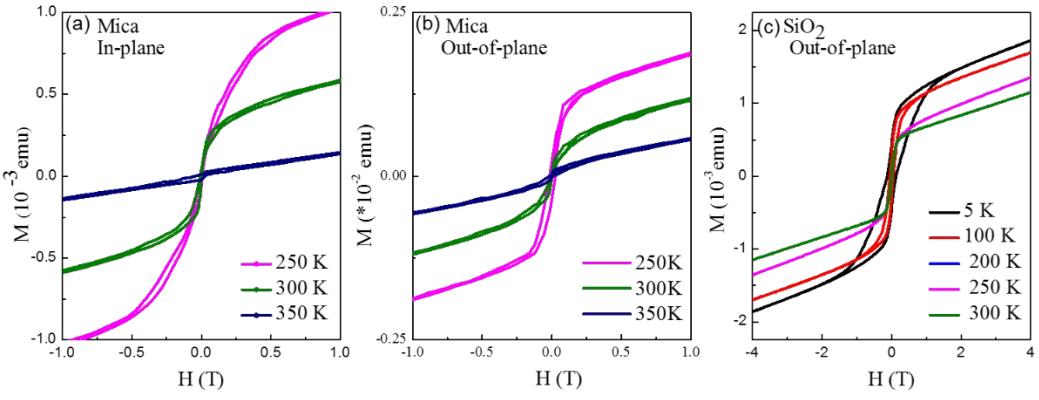

Figure S8. (a,b) Field-dependent magnetization at mica substrates in some special temperature with field from -7 T to 7 T for in-plane and out-of-plane, respectively. (c) Field-dependent magnetization at SiO_2 (out-of-plane).

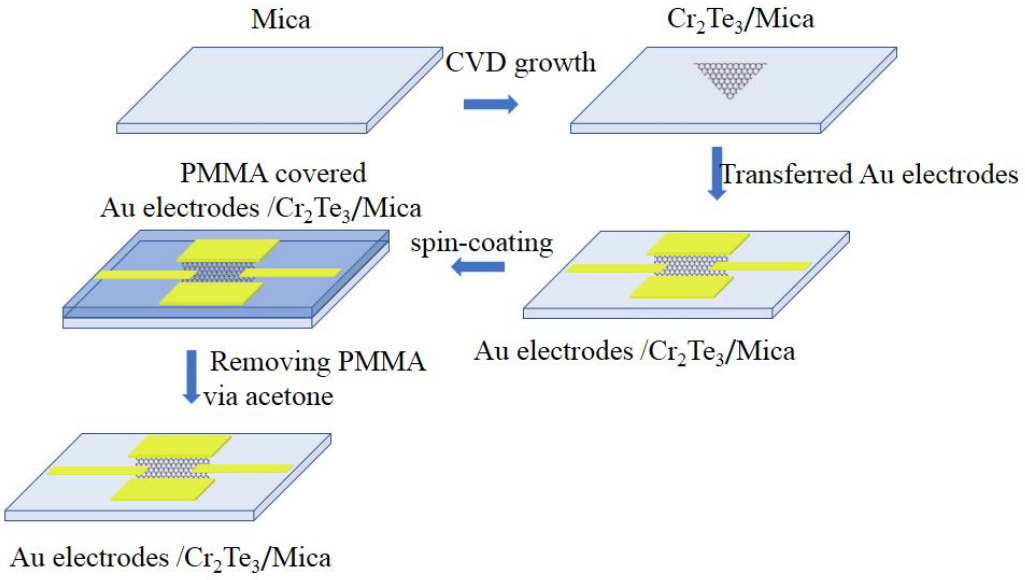

Figure S9. The flow chart of fabrication strategy. The devices are fabricated on top of a mica substrate indeed. The atomically flat Au electrodes with thickness of 150 nm is transferred to the Cr_2Te_3 flake of interest via probe. The probe adheres Au electrodes via Ga-In alloy, and then release the Au electrodes on target flakes. The atomically flat Au electrodes were fabricated by thermal evaporation via a shadow mask on SiO_2/Si substrates. Polymethyl methacrylate (PMMA) is spin-coated on the substrate which already contains the flake of interest and the Au on top. The PMMA spin-coated on devices can contribute to tight contact between Au electrodes and flakes, which may benefit by removing the bubble at interface between electrodes and flakes via spin-coating.

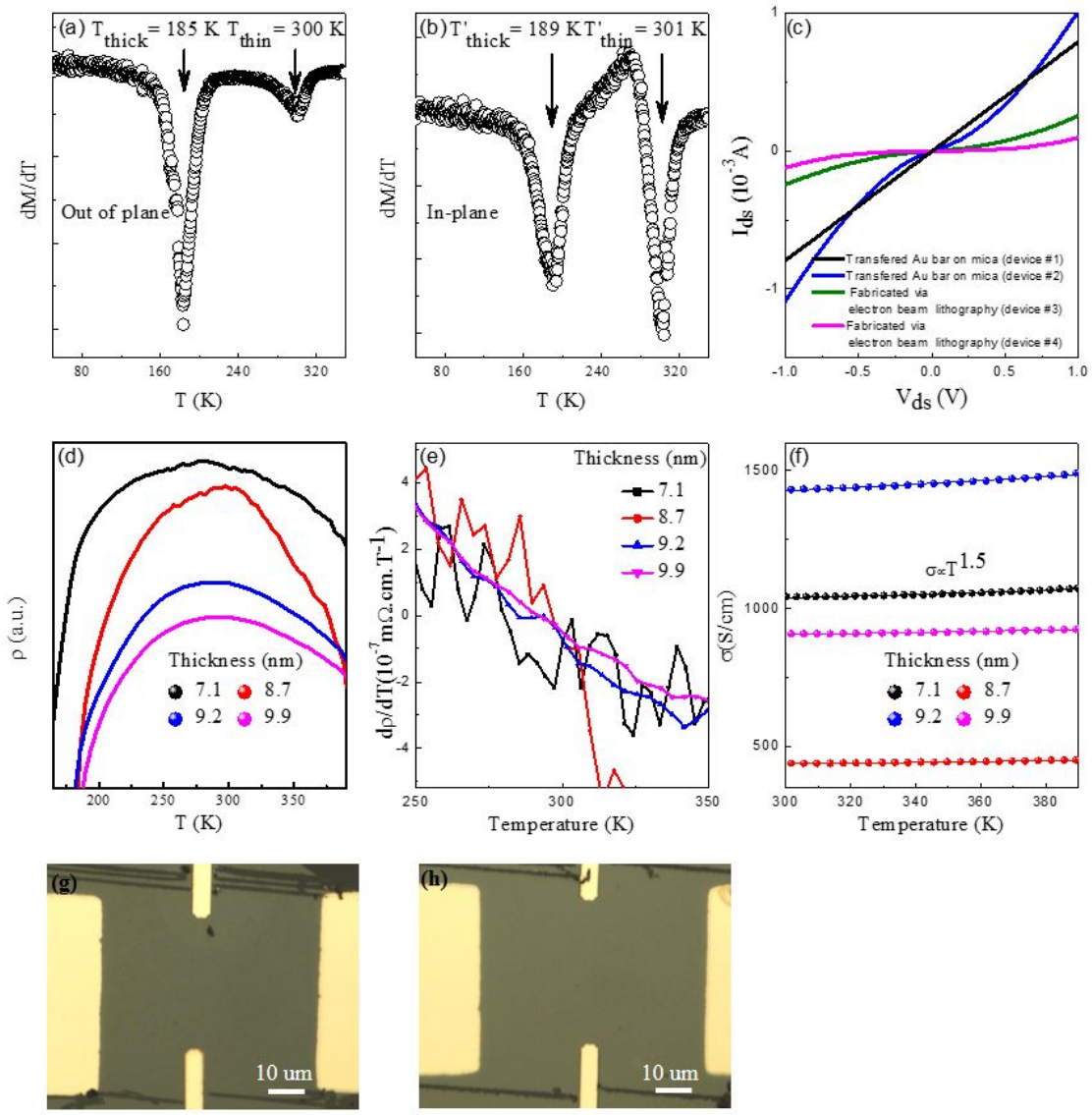

Figure S10. (a,b) Temperature-dependent of differential magnetic susceptibility (dM/dT) at mica substrates with a field 0.1 T for out-of-plane and in-plane, respectively. (c) Voltage bias-dependent drain current (I_{ds}-V_{ds}) curve. The Cr_2Te_3 is metallic as a result the advantage of achieving good electrical contact. However, when the devices were fabricated by a standard electron beam lithography process (EBL), the voltage bias-dependent drain current (I_{ds}-V_{ds}) curve exhibited obvious Schottky contact character as shown in **(c).** When the method of transferred Au electrodes was employed, and the I_{ds}-V_{ds} curve indicated the good electrical contact of the device. The EBL or thermal evaporation process are probable responsible for the Schottky barriers. The PMMA residue at the contact region can lead to additional barriers. The electronic beam irradiation during EBL process or metal atom bombardment at thermal evaporation process may damage the surface lattice. However, the methods of transferred electrodes

are not standardized processes, which will also result in Schottky contact character as shown in **(c)**. Therefore, the contact still impedes us achieve the channel resistance, which result in no obvious trend of R_{xx} with the thickness changed. As a result, the sample of 7.1 nm in thickness displays a lower resistivity than the 8.7 nm one owing to the contact problem. Realizing good electrical contact of 2D layers including graphene is still fundamental challenges.[1] (d) Temperature-dependent of electrical transport measurements of longitudinal resistance (R_{xx}) as thickness are varied. (e) Temperature-dependent of differential electrical resistivity (ρ_{xx}) as thickness are varied. The corresponding temperature of zero valued in differential electrical resistivity is defined as T_c. (f) Temperature-dependent σ can be well fitted by the power law ($\sigma \propto T^{1.5}$). Optical micrographs images of device structure with thickness of 5.5 (g) and 7.1 nm (h).

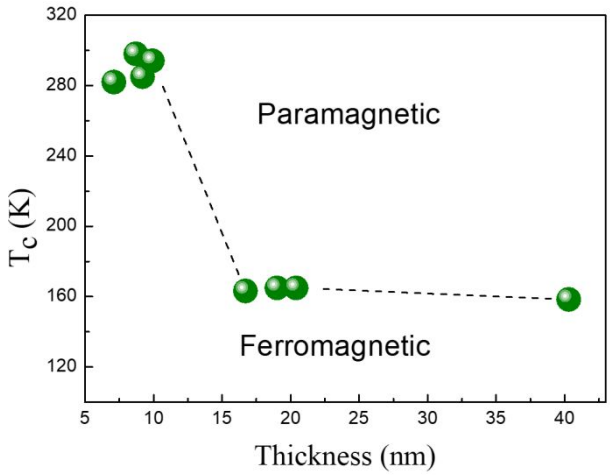

Figure S11. The Tc as a function of the thickness of Cr_2Te_3, extracted from position of the kink.

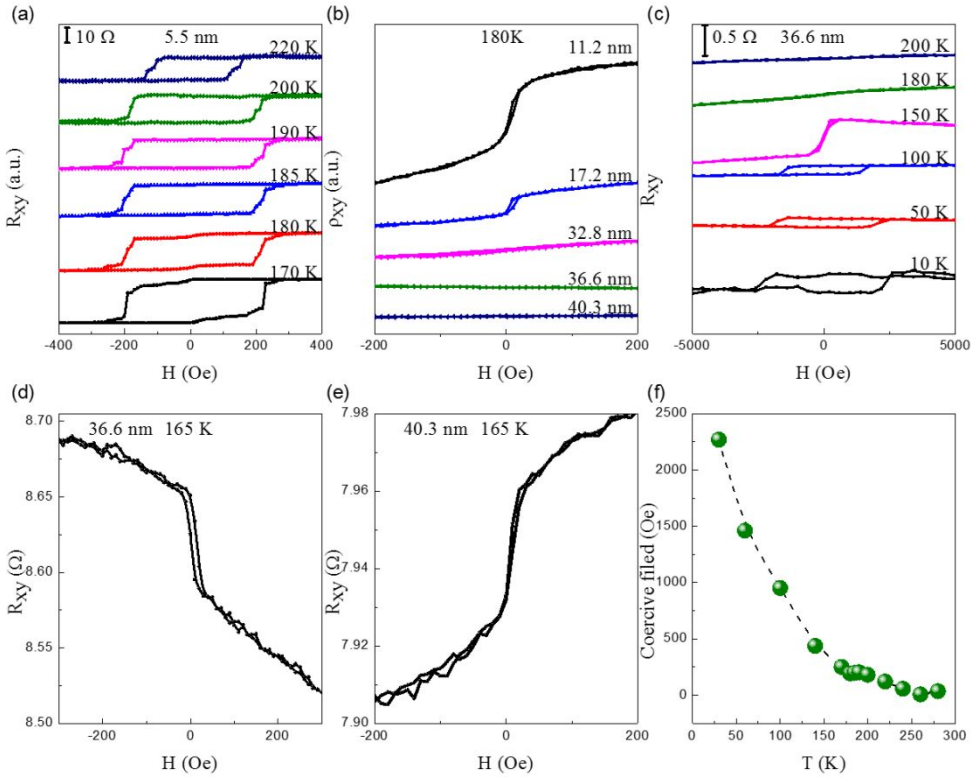

Figure S12. (a,c-e) H-dependent R_{xy} with different thickness and temperature. (b) External magnetic field (H) dependence Hall electrical resistivity ρ_{xy} as thickness are varied. (f) Temperature-dependent coercive field with the thickness of 5.5 nm.

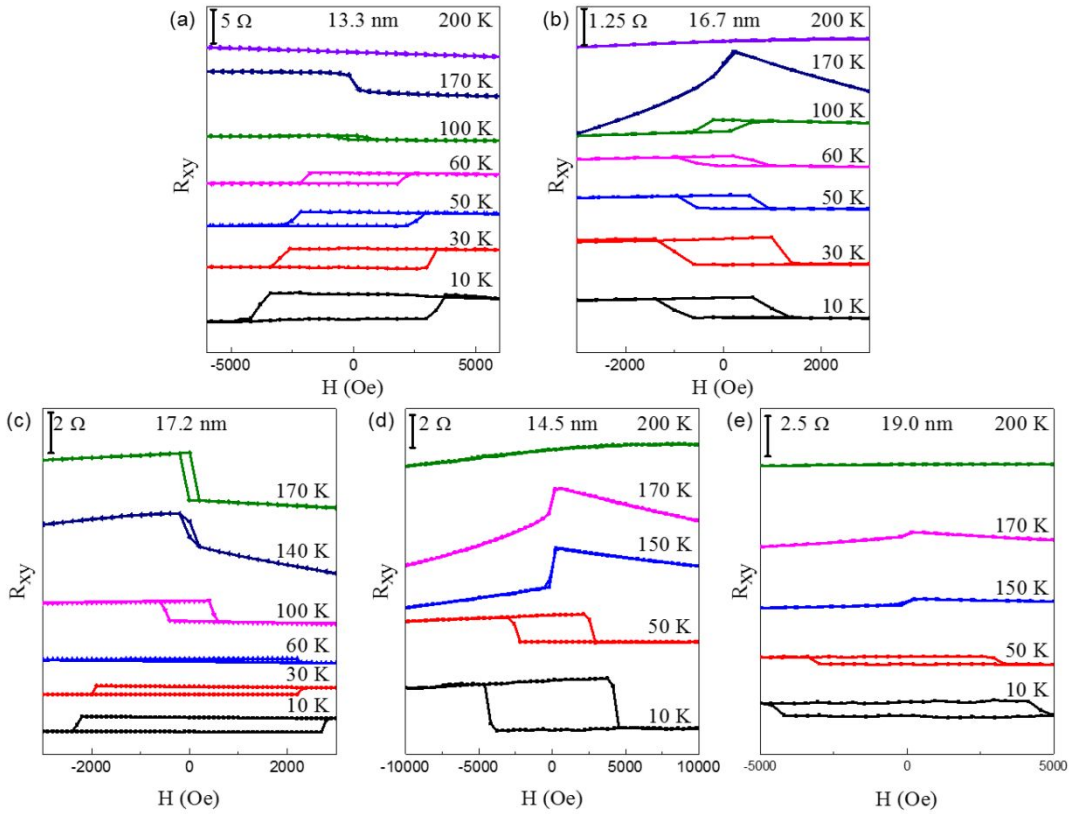

Figure S13. (a-f) H-dependent R_{xy} with different thickness and temperature.

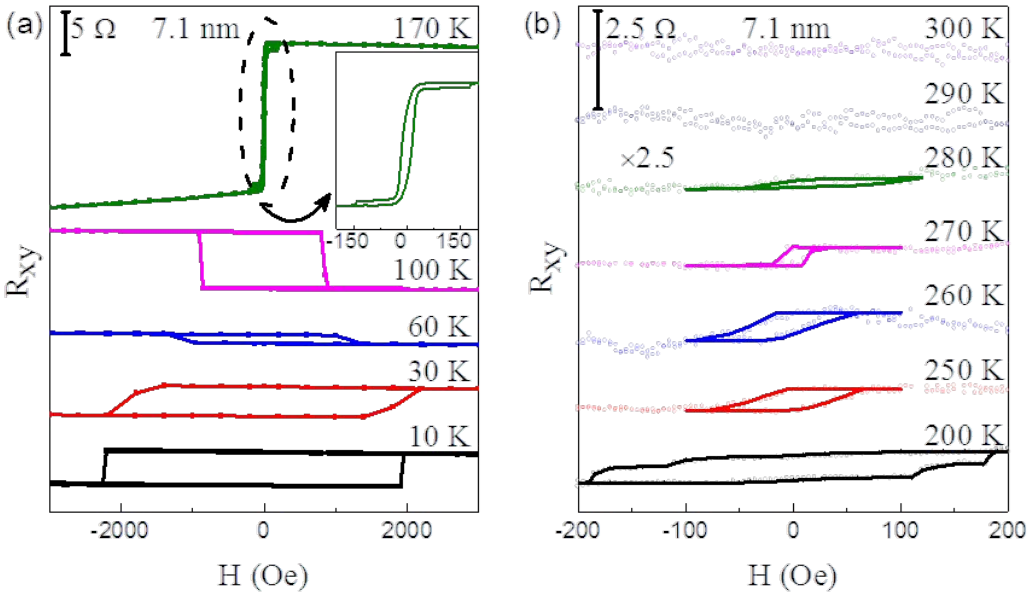

Figure S14. (a,b) H-dependent R_{xy} with thickness of 7.1 nm at different temperature. There is still hysteresis at 280 K, which provided an unambiguous evidence the existence of spontaneous magnetization at room temperature.

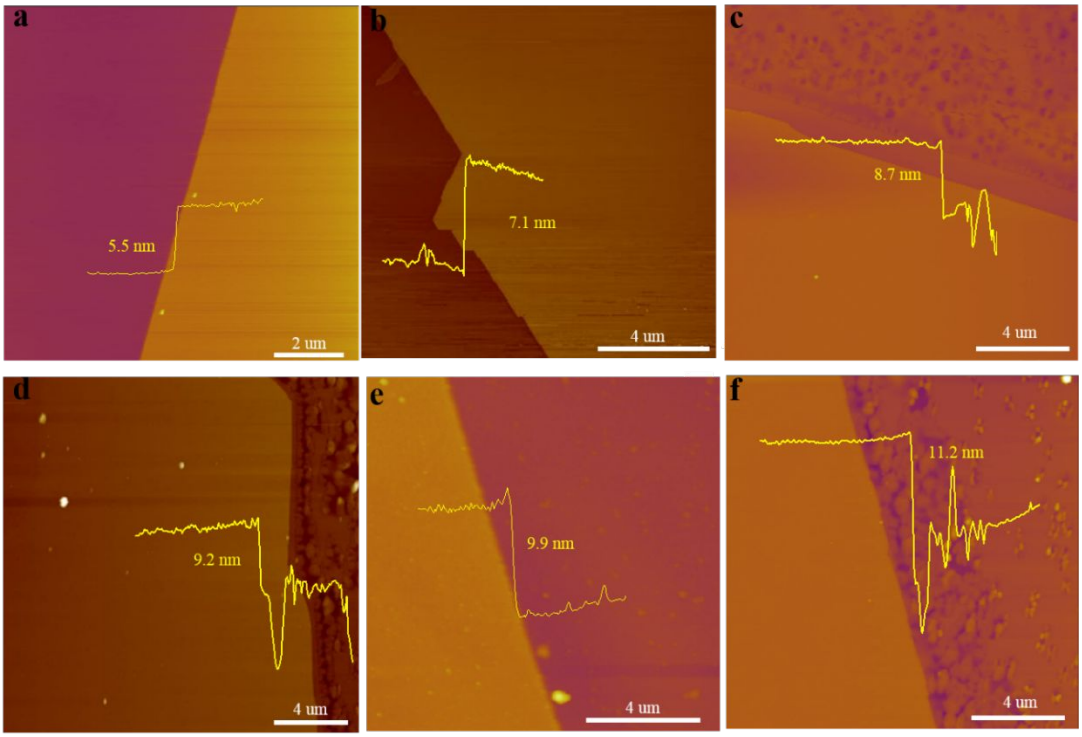

Figure S15. AFM images and height profile of devices.

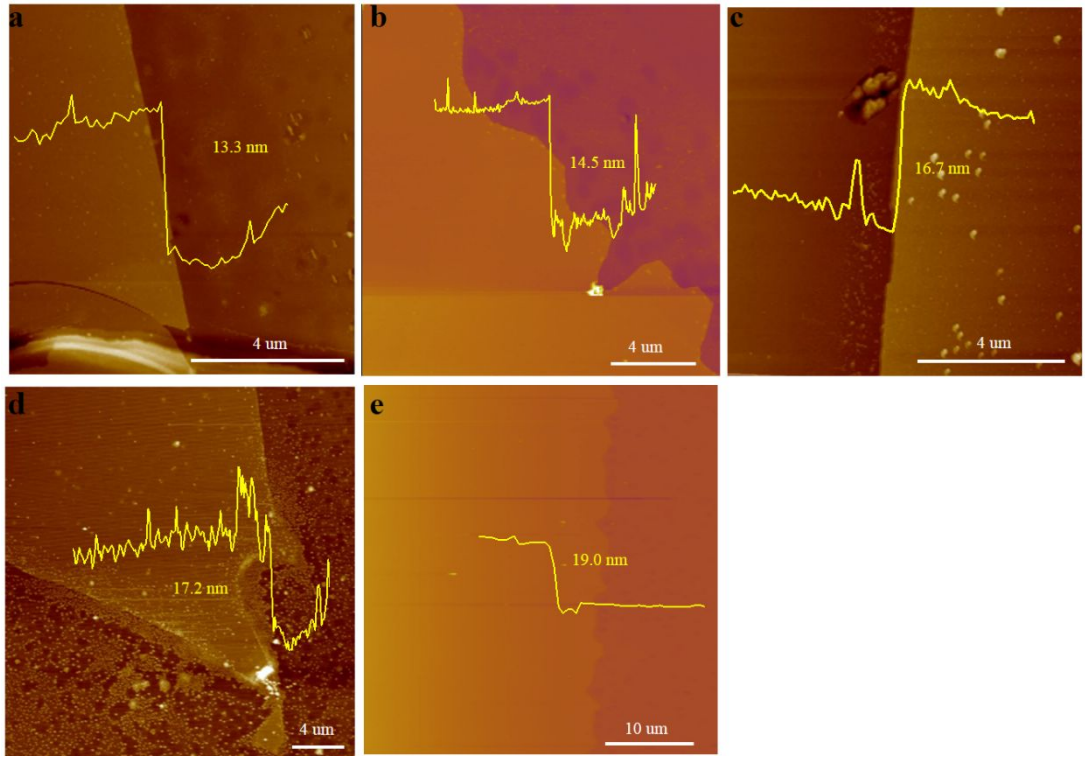

Figure S16. AFM images and height profile of devices.

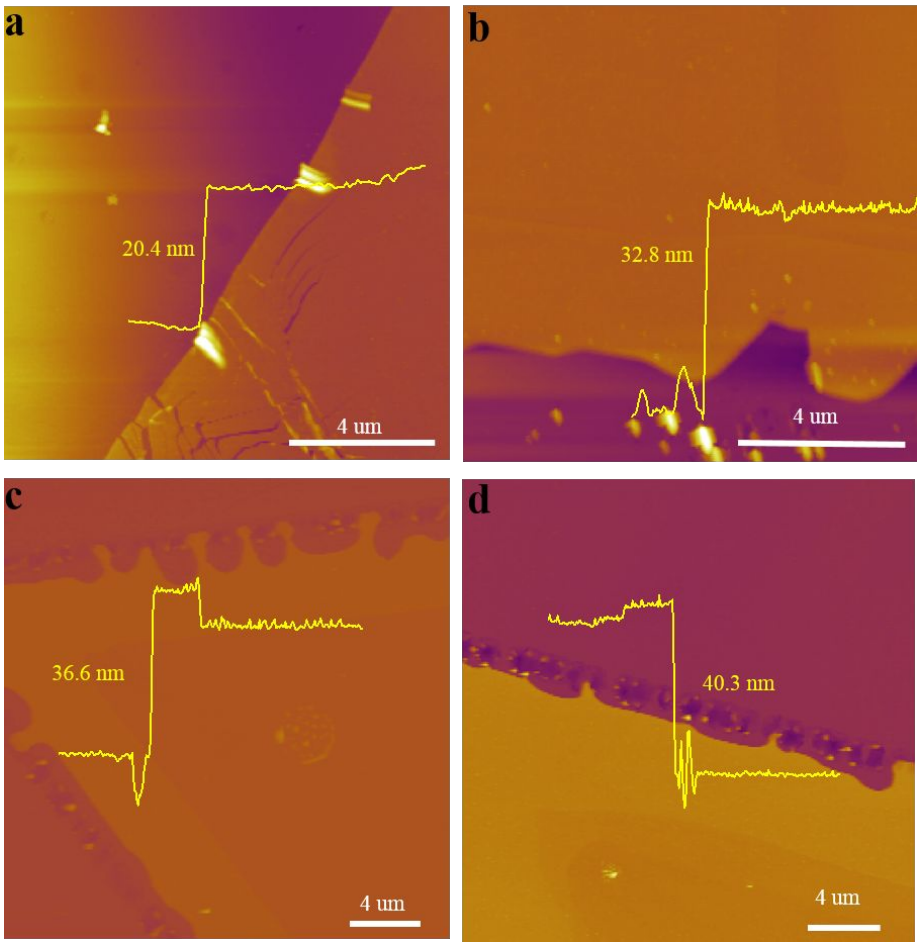

Figure S17. AFM images and height profile of devices.

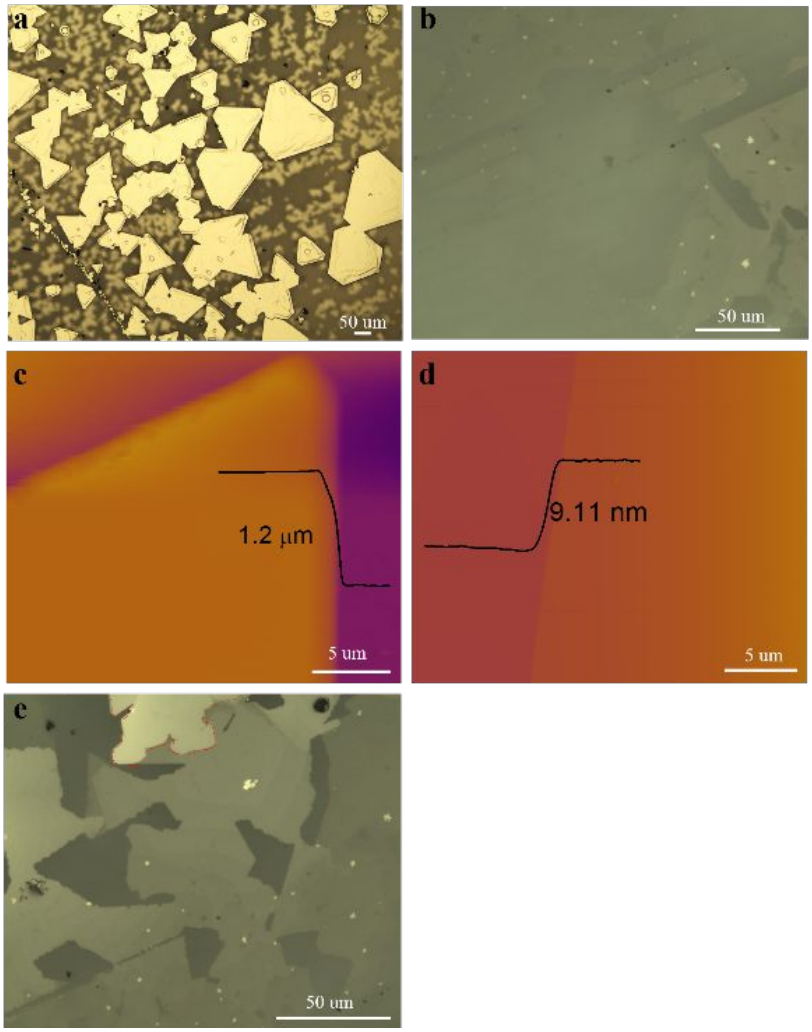

Figure S18. Optical micrographs image of CVD grown bulk (a) and 2D (b) Cr_2Te_3. AFM image of CVD grown bulk (c) and 2D (d) Cr_2Te_3. (e) The sample of 2D Cr_2Te_3 in XRD experiment. The area surrounded by the red line exhibits the sample in which the thickness is greater than 10 nm. For the synthesis of Cr_2Te_3, the mixture of $CrCl_3$ and NaCl were placed behind Te source at 850℃. The mica substrate was then kept near to $CrCl_3$ powder. The weight of $CrCl_3$ is approximately 10 mg. The bulk Cr_2Te_3 is easier to get when the weight of $CrCl_3$ increases to 500 mg. The precise control of sample thickness via CVD growth process have been extensive research. For example, the Cr_2S_3 can be accurately controlled to atomic thickness.[2] The selectivity of the synthetic process has been carefully analysed in recent work.[2] In our XRD experiment, the thickness of bulk Cr_2Te_3 is approximately 1 μm. Significantly, the thicknesses of 2D Cr_2Te_3 is far less than that of bulk Cr_2Te_3. In terms of crystal thickness of 2D limit in XRD analysis, the area ratio of the Cr_2Te_3, in which the thickness is less than 10 nm, is approximately 86.2%. The thickness of other samples in 2D Cr_2Te_3 is range from 10

to 20 nm. We define that the thickness of 2D Cr_2Te_3 is less than 10 nm in our experiments.

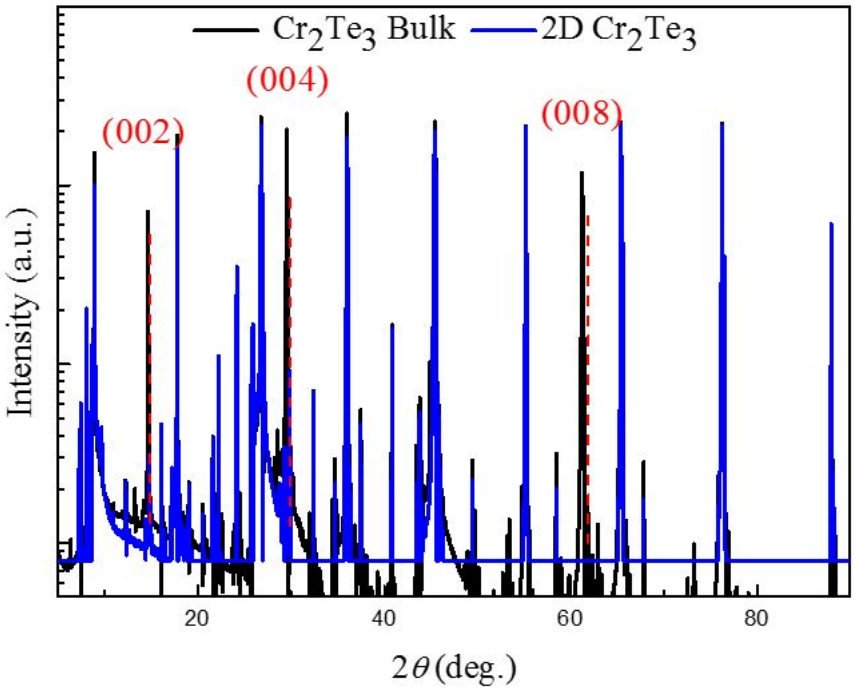

Figure S19. The XRD spectra of bulk and 2D Cr_2Te_3 on mica substrate.

From the XRD pattern, we can see that the peaks of 2D Cr_2Te_3 shift to right with a bigger angle (2θ) than bulk Cr_2Te_3, which is consistent with the claim that 2D Cr_2Te_3 exhibits a smaller value of lattice parameter than that of bulk Cr_2Te_3. Although we deducted the K_{a2} component from our XRD pattern by the Powder X program, there are some other peaks (maybe origin from the substrate) near (00l) peaks of 2D Cr_2Te_3. Limited by the quality of XRD data, we can't measure the width of XRD peaks accurately, so it is hard to clarify if there is a peak broadening at the XRD patterns of 2D and bulk Cr_2Te_3.

Our X-Ray source is non-monochromatic. After we deducted the K_{a2} component from our XRD pattern by the Powder X program, we find that there still seems to be unresolved doublets for 2D Cr_2Te_3, but singlet for bulk Cr_2Te_3 at low angle. We think the doublet in 2D Cr_2Te_3 contains other component which maybe originate from the substrate. First, the XRD have calibrated by XRD peak of mica substrates. Then, using the formula $2d\sin(\theta+\alpha) = j\lambda$ (α is the zero-shift error), a zero-shift error of 2D and bulk Cr_2Te_3 have been precluded by calculation.

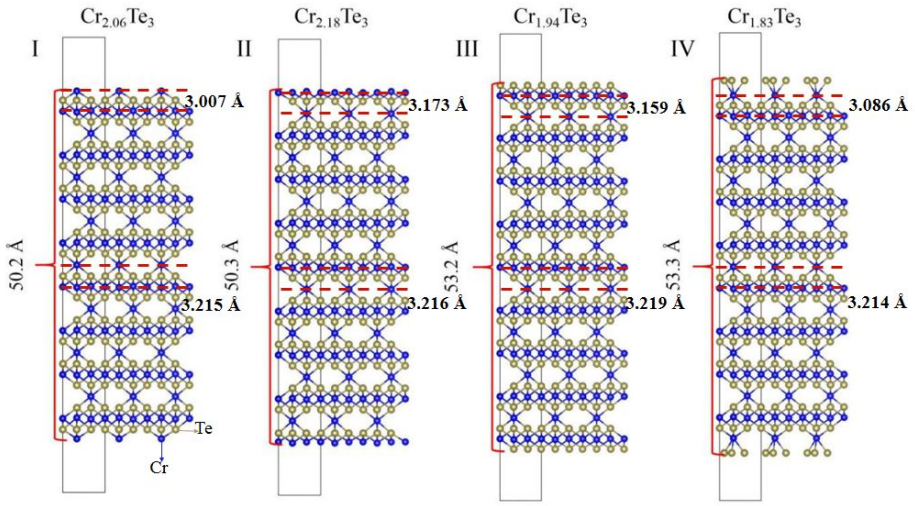

Figure S20. Four kinds of structures with different exposed atoms at the surface.

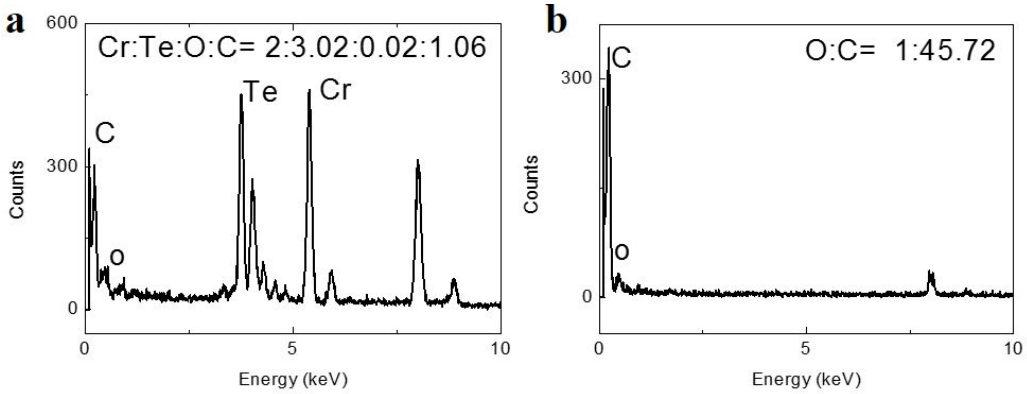

Figure S21. The chemical composition analysis of TEM-EDX. (a) Cr_2Te_3 domain on TEM grid with carbon film and (b) carbon film. When Cr atoms expose on the surface, the formation of CrO_x appear on the surfaces. The radius of O^{2-} is smaller than for Te^{2-}, which will compress the unit cell and thus enhance the Tc. We calculate the formation energy for achieving the stability of different exposed atoms. The results show that model III exhibits minimum formation energy. Therefore, the Te atoms expose on the surface, which is more stable. Furthermore, we also estimate the chemical composition via TEM-EDX analysis, and the stoichiometric ratio of Te and O is approximately 3.02:0.02 (a). Significantly, we have to take into consideration the content of oxygen element in carbon film substrates or organic residue as shown in (b). According to TEM-EDX results, we find that the content of oxygen element in Cr_2Te_3 is negligible. As a result, we speculate that the Tc is relatively unaffected by oxidation in our condition. The Te atoms exposed on the surface, which is more stable. Therefore, we

speculate that the oxidation is relatively small effect on reconstruction in our model.

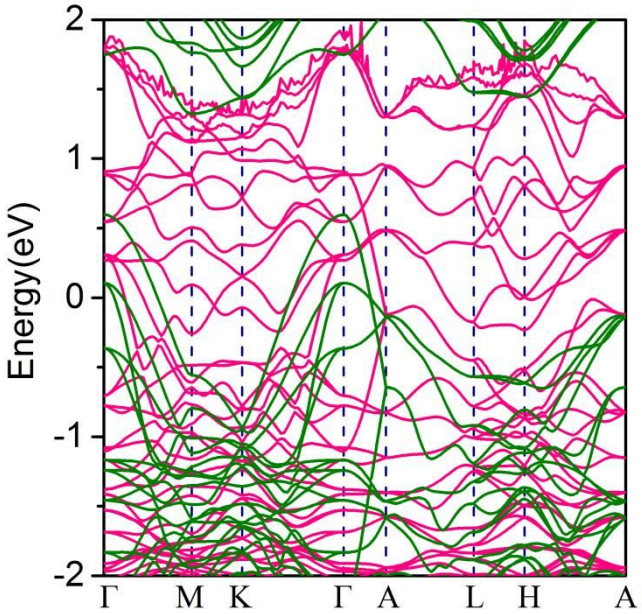

Figure S22. The band structure of the bulk Cr_2Te_3. The red line represents spin-up band, the green line reprents spin-down band.

Table S1. The bond valence sum (BVS) calculation results.

1	$Cr\text{-}Te_1$	$Cr\text{-}Te_2$	$Cr\text{-}Te_3$
r_{ij}	2.721(*6)	2.717(*3)	2.753(*3)
S_{ij}	0.581	0.587	0.533
V_i	3.485	3.359	
2	$Cr\text{-}Te_1$	$Cr\text{-}Te_2$	$Cr\text{-}Te_3$
r_{ij}	2.721(*6)	2.717(*3)	2.753(*3)
S_{ij}	0.581	0.587	0.533
V_i	3.485	3.359	
3	$Cr\text{-}Te_1$	$Cr\text{-}Te_2$	
r_{ij}	2.717(*6)	2.727(*6)	
S_{ij}	0.587	0.572	
V_i	3.522	3.429	
4	$Cr\text{-}Te_1$	$Cr\text{-}Te_2$	$Cr\text{-}Te_3$
r_{ij}	2.721(*6)	2.717(*3)	2.753(*3)
S_{ij}	0.581	0.587	0.533
V_i	3.485	3.359	
5	$Cr\text{-}Te_1$	$Cr\text{-}Te_2$	$Cr\text{-}Te_3$
r_{ij}	2.721(*6)	2.717(*3)	2.753(*3)
S_{ij}	0.581	0.587	0.533
V_i	3.485	3.359	
Average valence	3.460		

The BVS values (V_i) were calculated using the formula $V_i = \sum_j S_{ij}$, and $S_{ij} = \exp[(r_0$-

r_{ij})/0.37]. The value of r_0= 2.52 for Cr^{3+}.[3]

Supplementary Note 1. Magnetic properties of Cr_2Te_3.

At the lowest temperature range, M appears to diverge, this phenomenon can be seen in many ferro(i)magnetic materials. [4-7] Now, we discuss more details about the diverged M: As shown in Figure 2b, a broad maximum is observed in $M_{ZFC}(T)$, and only a small decrease of magnetization is shown when measured with small magnetic field, which can be seen in many ferro(i)magnetic materials, such as ferrimagnetic spinel $NiFe_2O_4$, ferromagnetic perovskite $La_{2/3}Ca_{1/3}MnO_3$.[8,9] The results of magnetization measurements show typical ferromagnetic character, including a broad maximum in $M_{ZFC}(T)$, weak thermomagnetic irreversibility at a weak magnetic field as shown in Figure 2b. Furthermore, there is only Cr^{3+} ions in Cr_2Te_3, which indicates that Cr_2Te_3 is a ferromagnet. On the other hand, Cr_2Te_3 is a highly anisotropic system, the irreversible thermomagnetic behavior between $M_{ZFC}(T)$ and $M_{FC}(T)$ may be account for its anisotropy. [10, 11]

The decrease of susceptibility between ~280 and 200 K in the in-plane data, it is probably origin from the magnetic moment turn to [001] direction gradually when the temperature drops to about 200 K. Because if the magnetic moment turns to [001] direction with temperature decreasing, the projection of moment in ab plane (in-plane) will decrease, but increase along c axis (out-of-plane) direction, which is consistent with the measured data shown in Figure 2a. The origin of the decrease in susceptibility between 280 and 200 K attribute to the competition between the forming of magnetic order and orientation of magnetic moment. Meanwhile, on the other hand, the explanation that the decrease origin from the competition of antiferromagnetism in this temperature range is also reasonable, which can be used to explain the magnetic behavior: As the article described: [12, 13] Cr_2Te_3 exhibit ferromagnetic superexchange between the Cr^{3+} centers in the planes, the moment is along c axis direction, and antiferromagnetic coupling within the interstitial Cr^{3+} ions. If the antiferromagnetic coupling is within ab plane (in-plane), the magnetic moment within ab plan (in-plane) will decrease. At the same time, because a ferromagnetic order forms near c axis (out-of-plane) direction in this temperature range, the value of M will increase in this direction as the temperature decreasing, which also consistent with the measured data. Based on these facts, the explanation that the special magnetic behavior may be origin from the competition of ferromagnetic and antiferromagnetic order at the temperature

range 200 K~280 K is also reasonable.

According to the early neutron studies, [12] our Cr_2Te_3 sample has the same crystal structure with that the paper mentioned above. Because our Cr_2Te_3 samples are too small to measure the neutron powder diffraction, we do not know the exactly magnetic structure. But from the magnetic data, we can see that along [001] direction, our sample be of ferromagnetism probably origin from the Cr^{3+} centres in the planes (00l), similar to that mentioned in the paper above. Besides, according to the magnetization data, we estimate the value of net ferromagnetic moment to be about 0.6 μ_B per Cr^{3+} ion at 2 K. Although this value is not so accurate due to the effect of substrate, it indicates strong ferromagnetic-like feature. Therefore, the current Cr_2Te_3 films tend to form long-range ferromagnetic order, in agreement with the article (H.Haraldsen et al). [12, 13] Of cause, in addition to the dominant ferromagnetic coupling, some antiferromagnetic or antisymmetric interactions are also possible to occur since the magnetic moment mentioned above is apparently less than the theoretical one for a Cr^{3+} ion with t_{2g}^3 configuration (3.0 μ_B).

As for the anisotropy parameter K, because the Cr_2Te_3 flakes randomly distributes on the mica substrate, we cannot get the saturated moments along [100] and [010] directions, so it is hard to calculate the exactly value of anisotropy parameter K.

Supplementary Note 2. The mechanism of magnetic transition

In order to exclude the mechanism of the room temperature magnetic transition origins from the substrate or the interaction between the substrate and the sample, different samples in which substrate were mica and SiO_2 were measured. Both of them have the ferromagnetic-like behavior. We can exclude that the mechanism of the room temperature magnetic transition origins from the samples to be oxidized into Cr_2O_3, CrO_2 or CrO_3. Considering different Cr_2O_3 films will occur an antiferromagnetic or ferrromagnetic transition at about 296 K and 50 K, respectively,[14, 15]so the ferromagnetic-like transition occurred at about 300 K is not from Cr_2O_3. As for CrO_2 thin film, the ferromagnetic transition temperature is about 390K, [16] So the room

temperature transition is not from CrO_2 too. Finally, considering the high valence Cr^{6+} in CrO_3 must be synthesized by some special strong oxidant, like concentrated sulfuric acid, and usually the interaction needs to have a high temperature environment. Besides, the valence state of Cr in Cr_2Te_3 is near +3 from the BVS calculation results (the detail information sees Extended Data Table 1). Based on those facts, in the room temperature, there is a low possibility that room temperature magnetic transition origins from CrO_3. Al doping results in n-type Cr_2Te_3, in which the T_c is 244 K. [17] In our case, the Cr_2Te_3 is p-type. These provide strong evidence that Al doping mechanism does not dominate the underlying mechanism.

Supplementary Note 3. Fabrication of devices

The single-unit-cell Cr_2Te_3 exhibits insulator characteristic with huge resistance, which may derive from structural instability or reconstruction of entire structure. The resistance is beyond the range of PPMS measurement. We employed polar reflective magnetic circular dichroism (RMCD) to monitor the magnetism. However, the RMCD signal is very weak which may originate from substrate noise. As mentioned before, the transfer of crystals can result in the damage of sample, especially in thin sample.

In order to guarantee the uniform number of layers, we firstly identify the different layers via optical microscope and atomic force microscope (AFM) measurement as shown in Figure S15-17. According to the different contrast of optical microscope and AFM images, height profile of devices, we can easily identify the different layers. Then, the probe with diameter of 1μm was used to fabricate faint cracks, which can segregate different layers and guarantee the uniform number layers of devices. In our condition, the edge of Cr_2Te_3 may cause continuous thicker layers, in which the probe can fabricate faint cracks for guaranteeing the uniform number layers of devices.

Supplementary Note 4. The electrical transport measurements of longitudinal resistance (R_{xx})

When the dimensionality drops to 9.9 nm, the Cr_2Te_3 shows classical semiconducting behavior that the electrical resistivity increases with decreasing temperature in the high-temperature range (294-390 K) (Figure S10 d). However, when the temperature is lower

than 294 K, the electrical resistivity decreases with decrease in temperature which accounts for obvious metallic behavior in Cr_2Te_3. The magnetic scattering is usually ascribed to the exchange interaction between free carrier and localized magnetic electrons. [18] The magnetic scattering will sharply reduce after magnetic order occurring. Therefore, we can roughly estimate the T_c according the change of longitudinal resistance (R_{xx}). The weak change of R_{xx} with the thickness changed will not hinder the trends of that as temperature change. The metallic behavior may originate from reducing magnetic scattering after magnetic order occurring. The corresponding temperature of zero valued in differential electrical resistivity is defined as T_c. The transition temperature may derive from reduced magnetic scattering as a consequence of spontaneous magnetization. We further extracted Tc from position of the kink. The T_c is around 294 K with thickness of 9.9 nm (Figure S10 e). With the subsequent reduction of thickness to 9.2, 8.7 and 7.1 nm, the same phenomenon was observed, and we can roughly extract the T_c about 285, 298, 282 K respectively (Figure S10 e). Interestingly, this value is consistent with the χ-T and M-H data obtained from magnetization measurements. We speculate the room temperature ferromagnetism results from ultrathin flakes (thinner than around 9.9 nm). Below 9.9 nm dimensionality, the ultrathin Cr_2Te_3 exhibit a classical semiconducting behavior where the conductivity (σ) increases with increasing temperature between 300 and 390 K. As clearly depicted in Figure S10 f, the temperature-dependent σ can be well fitted by the power law ($\sigma \propto T^{1.5}$). Irrespective to change in carrier densities, we can speculate that the impurity scattering mechanisms strongly dominate electronic transport in the high temperature range (300-390 K). [19] The semiconducting behavior observed in thinner Cr_2Te_3 may originate from opening up of a bandgap. [20] The quantum confinement effects in 2D limit can induce a gap. [21-23] The magnetically induced gapped-insulator surfaces phase was also observed via an angle-resolved photoemission spectroscopy (ARPES) in topological insulator. The quantum confinement effects or magnetic induced gap can distinguish from measurement the spin texture at the time-reversal (TR)invariant moment, because the spins are doubly

degenerate at the TR invariant momenta with the unbroken the TR symmetry via Kramers' degeneracy theorem. In our specific case, Cr_2Te_3 turned into a paramagnetic order over 300 K, while the semiconducting behavior appeared at the high temperature range (300-390 K). As a result, we can roughly exclude the magnetically induced gap. Furthermore, in consideration of the conductivity ($\sigma < 10^4\ \Omega^{-1}\ cm^{-1}$), the bad-metal regime indicates a strong disorder of the thin films. [24] The strong spatial fluctuations and thermal disorder of surface can also induce a gap. [22, 25]

The position of kink in longitudinal resistance experiences was extracted, as shown in Figure S11. It is consistent with the Hall result; the Tc of Cr_2Te_3 increases when its thickness decrease. However, the Hall results are more precise for extracting Tc in our condition. When the thickness of Cr_2Te_3 is less than the 2D limit, the kink around 180 K still appears. We speculate that the Cr_2Te_3 below the 2D limit exhibits two magnetic phase transitions: one is at about 300 K, and another is at about 180 K. This is the reason why the anomaly is not disappearing below the 2D limit in accordance with the Curie temperature (Tc) observed. The kink observed at near 300 K is extremely broad, and in addition the differential trace is extremely noisy. We think it may be origin from the forming of short-range magnetic order at around 300 K before the forming of long-range ferromagnetic order. For the anomaly at about 180 K, the resistance decreased sharply, which probably account for the occurrence of long-range magnetic order rapidly.

REFERENCES

1. Wang, L.; Meric, I.; Huang, P. Y.; Gao, Q.; Gao, Y.; Tran, H.; Taniguchi, T.; Watanabe, K.; Campos, L. M.; Muller, D. A.; Guo, J.; Kim, P.; Hone, J.; Shepard, K. L.; Dean, C. R. One-dimensional electrical contact to a two-dimensional material. *Science* **2013,** *342*, 614-617.

2. Cui, F.; Zhao, X.; Xu, J.; Tang, B.; Shang, Q.; Shi, J.; Huan, Y.; Liao, J.; Chen, Q.; Hou, Y.; Zhang, Q.; Pennycook, S. J.; Zhang, Y. Controlled growth and thickness-dependent conduction-type transition of 2D ferrimagnetic Cr_2S_3 Semiconductors. *Adv.*

Mater. **2020,** *32*, 1905896.

3. Brese, N. E.; Okeeffe, M. Bond-valence parameters for solids. *Acta Crystallographica Section B-Structural Science* **1991,** *47*, 192-197.

4. Wang, X.; Liu, M.; Shen, X.; Liu, Z.; Hu, Z.; Chen, K.; Ohresser, P.; Nataf, L.; Baudelet, F.; Lin, H.-J.; Chen, C.-T.; Soo, Y.-L.; Yang, Y.-f.; Jin, C.; Long, Y. High-temperature ferrimagnetic half metallicity with wide spin-up energy gap in $NaCu_3Fe_2Os_2O_{12}$. *Inorg. Chem.* **2019,** *58*, 320-326.

5. Feng, H. L.; Arai, M.; Matsushita, Y.; Tsujimoto, Y.; Guo, Y.; Sathish, C. I.; Wang, X.; Yuan, Y.-H.; Tanaka, M.; Yamaura, K. High-temperature ferrimagnetism driven by lattice distortion in double perovskite Ca_2FeOsO_6. *J. Am. Chem. Soc.* **2014,** *136*, 3326-3329.

6. Deng, H.; Liu, M.; Dai, J.; Hu, Z.; Kuo, C.; Yin, Y.; Yang, J.; Wang, X.; Zhao, Q.; Xu, Y.; Fu, Z.; Cai, J.; Guo, H.; Jin, K.; Pi, T.; Soo, Y.; Zhou, G.; Cheng, J.; Chen, K.; Ohresser, P.; Yang, Y.-f.; Jin, C.; Tjeng, L.-H.; Long, Y. Strong enhancement of spin ordering by A-site magnetic ions in the ferrimagnet $CaCu_3Fe_2Os_2O_{12}$. *Phys. Rev. B* **2016,** *94*, 024414.

7. Byeon, S.-H.; Lee, S.-S.; Parise, J. B.; Woodward, P. M.; Hur, N. H. New ferrimagnetic oxide $CaCu_3Cr_2Sb_2O_{12}$: High-pressure synthesis, structure, and magnetic properties. *Chem. Mater.* **2005,** *17*, 3552-3557.

8. Kumar, P. A.; Shrotri, J.; Kulkarni, S.; Deshpande, C.; Date, S. Low temperature synthesis of $Ni_{0.8}Zn_{0.2}Fe_2O_4$ powder and its characterization. *Mater. Lett.* **1996,** *27*, 293-296.

9. Anil, K. S.; Alias, J.; Date, S. Effect of compositional homogeneity on the magnetic propertiesof $La_{0.7}$ $Ca_{0.3}$ MnO_3. *J. Mater. Chem.* **1998,** *8*, 1219-1223.

10. Kumar, P. A.; Joy, P.; Date, S. On the irreversible magnetic behavior of the anisotropic ferromagnetic system $SrRuO_3$. *Physica B: Condensed Matter* **1999,** *269*, 356-361.

11. Joy, P.; Date, S. Unusual magnetic hysteresis behavior of oxide spinel $MnCo_2O_4$. *J. Magn. Magn. Mater.* **2000,** *210*, 31-34.

12. Haraldsen, H.; Neuber, A. *Z.* A. Magnetochemische untersuchungen. XXVII. magnetische und röntgenographische untersuchungen am system chrom–tellur. *Anorg. Allg. Chem.* **1937,** *234*, 353-371.

13. Goodenough, J. B. Types of Magnetic Order. In *Magnetism and the Chemical Bond;* Cotton, F. A.; Interscience Publishers Inc.: New York, 1963; Vol. I, pp 75-156.

14. Qiu, Z.; Hou, D.; Barker, J.; Yamamoto, K.; Gomonay, O.; Saitoh, E. Spin colossal magnetoresistance in an antiferromagnetic insulator. *Nat. Mater.* **2018,** *17*, 577-580.

15. Halley, D.; Najjari, N.; Majjad, H.; Joly, L.; Ohresser, P.; Scheurer, F.; Ulhaq-Bouillet, C.; Berciaud, S.; Doudin, B.; Henry, Y. Size-induced enhanced magnetoelectric effect and multiferroicity in chromium oxide nanoclusters. *Nat. Commun.* **2014,** *5*, 3167.

16. Keizer, R. S.; Goennenwein, S. T. B.; Klapwijk, T. M.; Miao, G.; Xiao, G.; Gupta, A. A spin triplet supercurrent through the half-metallic ferromagnet CrO_2. *Nature* **2006,** *439*, 825.

17. Li, H.; Wang, L.; Chen, J.; Yu, T.; Zhou, L.; Qiu, Y.; He, H.; Ye, F.; Sou, I. K.; Wang, G. Molecular beam epitaxy grown Cr_2Te_3 thin films with tunable curie temperatures for spintronic devices. *ACS Appl. Nano Mater.* **2019,** *2*, 6809-6817.

18. Kamalakar, M. V.; Raychaudhuri, A. K. Low temperature electrical transport in ferromagnetic Ni nanowires. *Phys. Rev. B* **2009,** *79*, 205417.

19. Cui, X.; Lee, G.-H.; Kim, Y. D.; Arefe, G.; Huang, P. Y.; Lee, C.-H.; Chenet, D. A.; Zhang, X.; Wang, L.; Ye, F.; Pizzocchero, F.; Jessen, B. S.; Watanabe, K.; Taniguchi, T.; Muller, D. A.; Low, T.; Kim, P.; Hone, J. Multi-terminal transport measurements of MoS_2 using a van der Waals heterostructure device platform. *Nat. Nanotechnol.* **2015,** *10*, 534-540.

20. Niu, J.; Yan, B.; Ji, Q.; Liu, Z.; Li, M.; Gao, P.; Zhang, Y.; Yu, D.; Wu, X. Anomalous Hall effect and magnetic orderings in nanothick V_5S_8. *Phys. Rev. B* **2017,** *96*, 075402.

21. Sprinkle, M.; Ruan, M.; Hu, Y.; Hankinson, J.; Rubio-Roy, M.; Zhang, B.; Wu, X.; Berger, C.; de Heer, W. A. Scalable templated growth of graphene nanoribbons on SiC.

Nat. Nanotechnol. **2010,** *5*, 727.

22. Xu, S.-Y.; Neupane, M.; Liu, C.; Zhang, D.; Richardella, A.; Andrew Wray, L.; Alidoust, N.; Leandersson, M.; Balasubramanian, T.; Sánchez-Barriga, J.; Rader, O.; Landolt, G.; Slomski, B.; Hugo Dil, J.; Osterwalder, J.; Chang, T.-R.; Jeng, H.-T.; Lin, H.; Bansil, A.; Samarth, N.; Zahid Hasan, M. Hedgehog spin texture and Berry's phase tuning in a magnetic topological insulator. *Nat. Phys.* **2012,** *8*, 616.

23. Deng, Y.; Yu, Y.; Song, Y.; Zhang, J.; Wang, N. Z.; Sun, Z.; Yi, Y.; Wu, Y. Z.; Wu, S.; Zhu, J.; Wang, J.; Chen, X. H.; Zhang, Y. Gate-tunable room-temperature ferromagnetism in two-dimensional Fe_3GeTe_2. *Nature* **2018,** *563*, 94-99.

24. Nagaosa, N.; Sinova, J.; Onoda, S.; MacDonald, A. H.; Ong, N. P. Anomalous Hall effect. *Rev. Mod. Phys.* **2010,** *82*, 1539-1592.

25. Beidenkopf, H.; Roushan, P.; Seo, J.; Gorman, L.; Drozdov, I.; Hor, Y. S.; Cava, R. J.; Yazdani, A. Spatial fluctuations of helical Dirac fermions on the surface of topological insulators. *Nat. Phys.* **2011,** *7*, 939.